Journal of Computer Assisted Tomography
26(5):701–710

Detection of Hypervascular Hepatocellular Carcinoma: Comparison of SPIO-enhanced MRI With Dynamic Helical CT

Masatoshi Hori, Takamichi Murakami, Tonsok Kim, Kyo Tsuda, Satoru Takahashi,
Atsuya Okada, Manabu Takamura, and Hironobu Nakamura

Purpose: The purpose of this study was to compare the diagnostic performance of superparamagnetic iron oxide (SPIO)-enhanced MRI for the detection of hypervascular hepatocellular carcinoma (HCC) with dynamic helical CT.

Methods: SPIO-enhanced MR and dynamic helical CT images obtained from 41 patients with 52 hypervascular HCCs (5–130 mm; mean, 27 mm) were retrospectively analyzed. MRI were obtained with 1.5 T scanners using T2-weighted and proton density-weighted spin-echo (or fast spin-echo) sequences for all cases and a T2*-weighted gradient echo sequence for 36 cases. Four blinded observers reviewed images independently. Diagnostic accuracy was evaluated using alternative-free response receiver operating characteristic (AFROC) method. Sensitivities and positive predictive values (PPV) were also evaluated.

Results: The areas under the AFROC curves for each observer were greater for MR than for CT (means, 0.81 and 0.76; $p < 0.05$). The mean sensitivities for MR and CT were 0.75 and 0.71, respectively ($p = 0.13$). The mean PPVs were 0.83 and 0.79 ($p = 0.21$).

Conclusion: SPIO-enhanced MRI showed slightly better diagnostic performance than dynamic helical CT for the detection of hypervascular HCCs.

Index Terms: Liver neoplasms—Magnetic resonance (MR)—Computed tomography (CT)—Comparative studies—Receiver operating characteristic curve (ROC).

Superparamagnetic iron oxide (SPIO) is a liver-specific particulate MR contrast agent that is taken up by the reticuloendothelial system of the liver and improves the focal hepatic lesion-to-liver contrast-to-noise ratio and hepatic tumor detection. Some researchers (1–3) have compared the capability of SPIO-enhanced MRI with that of dynamic helical CT for detecting malignant hepatic lesions and have found SPIO-enhanced MRI to be superior. In those studies, however, most of the subjects had metastatic liver tumors. To our knowledge, few studies have been conducted to compare SPIO-enhanced MRI with dynamic helical CT in terms of hepatocellular carcinoma (HCC) detection capability.

Hepatocellular carcinoma is the most common primary malignant hepatic neoplasm and usually occurs in patients with chronic liver disease. Because cirrhotic liver tissue shows less response to SPIO particles than does healthy liver tissue (4), the diagnostic capability of SPIO-enhanced MRI for HCC detection may be limited. Tang et al. (5) found SPIO-enhanced MRI to be less accurate than dynamic gadolinium-enhanced MRI. Moreover, compared with dynamic gadolinium-enhanced MRI, dynamic helical CT is thought to have similar (6) or slightly inferior (7) diagnostic capability for detecting HCC. Thus, SPIO-enhanced MRI may be less accurate than dynamic helical CT for HCC detection.

The purpose of this study was to compare the diagnostic accuracy of SPIO-enhanced MRI with that of dynamic helical CT for the detection of hypervascular HCC by using alternative-free response receiver operating characteristic (AFROC) analysis with multiple readers.

METHODS

Patients

Between August 1995 and December 1999, 90 patients suspected of having HCC based on previously performed sonography or elevated tumor marker levels of

---

From the Department of Radiology, Osaka University Graduate School of Medicine, Osaka, Japan. Address correspondence and reprint requests to Dr. M. Hori at Department of Radiology, Osaka University Graduate School of Medicine, D1, 2–2, Yamadaoka, Suita-city, Osaka 565-0871, Japan. E-mail: mhori@radiol.med.osaka-u.ac.jp

serum alpha-fetoprotein or protein induced in vitamin K absence (PIVKA)-II underwent SPIO-enhanced MRI at our department. For 59 of these patients, three imaging modalities—SPIO-enhanced MRI, dynamic helical CT, and digital subtraction angiography with angiographically assisted helical CT (CT during arterial portography, CT hepatic arteriography, or iodized oil CT)—were performed within 30 days. Informed consent for the examinations was obtained from all patients. Eighteen of the 59 patients were excluded from our study because (1) there were neither sufficient follow-up examinations nor surgery to determine the true lesions (n = 16) or (2) there were too many nodules (more than 10 in one patient) to be analyzed (n = 2). The remaining 41 patients (34 men and 7 women), aged 49–81 years (mean, 64 years), were included in this retrospective study. Five of these patients had no HCC lesions as confirmed by follow-up studies lasting more than 1 year. Twenty of the 41 patients underwent definitive surgery with intraoperative sonography within 40 days of MRI, CT, and angiography. For 6 of the remaining 16 patients who had a clinical history of surgical resection of HCC, recurrent postoperative HCC was diagnosed on the basis of their clinical course. Two patients were diagnosed at autopsy, and three patients underwent sonography-guided needle core aspiration biopsy of at least one liver tumor for histologic evidence of HCC. As for the latter, other tumors with imaging findings similar to those of the histologically evaluated lesions were considered to be of the same disease. For five patients without histopathologic evidence of disease, the visible hepatic tumors were considered to be HCC based on tumor growth observed at follow-up examinations and on increased levels of serum alpha-fetoprotein or PIVKA-II.

Of the 41 patients entered into this study, 23 had hepatic cirrhosis. Eight were diagnosed on the basis of clinical examinations and blood chemistry tests, and 15 were diagnosed based on the evidence of pathologic specimens. Twenty-two of these patients had cirrhosis associated with viral hepatitis (8 patients with hepatitis B, 18 with hepatitis C, and 4 with both). The remaining one patient had neither viral cirrhosis nor ethanol-induced cirrhosis. Of the 18 patients without cirrhosis, 17 had chronic hepatitis (6 with hepatitis B, 13 with hepatitis C, and 3 with both), and 1 had neither viral hepatitis nor ethanol-induced hepatitis. Severity of the disease evaluated according to the Child-Pugh classification (8) showed 14 patients classified as class A (mild cirrhosis), 25 as class B (moderate cirrhosis), and 2 as class C (severe cirrhosis).

The presence or absence of hypervascular HCC lesions was decided by consensus of two radiologists other than four blinded readers based on findings obtained with digital subtraction angiography, CT during arterial portography, CT hepatic arteriography, iodized oil CT, sonography, dynamic CT, T1- and T2-weighted MRI, and dynamic gadolinium-enhanced MRI, and with follow-up sonography, CT, MRI, and definitive surgery with intraoperative sonography, biopsy, and serologic examination. The characteristics of hypervascularity were determined by means of angiography and angiographically assisted CT examinations. Cysts, hemangiomas, and other hypovascular lesions were excluded from our analysis. As a result, confirmation of 52 hypervascular HCC lesions (diameter, 5–130 mm; mean, 27 mm) was obtained for 36 of the 41 patients.

MRI

MRI was performed with a superconducting magnet operating at 1.5 T (Signa; GE Medical Systems, Milwaukee, WI, U.S.A., or Magnetom; Siemens, Erlangen, Germany). All MRI were obtained in the axial plane. For all pulse sequences, an 8 mm section thickness was used with a 2 mm intersection gap and a field of view of 30–32 cm. Presaturation pulses were applied at levels above and below the imaging volume to minimize the effect of flow artifacts.

For 33 of the 41 patients, unenhanced MRI, including T1-weighted and T2-weighted images, was performed. T1-weighted images were obtained with either a conventional spin-echo sequence (repetition time [TR] millisecond / echo time [TE] millisecond, 500/30; two signals acquired, 256 × 160–192 matrix) for 11 patients or a gradient echo sequence (repetition time [TR] millisecond / echo time [TE] millisecond / flip angle [FA] degree, 150/4.2/90; one signal acquired, 256 × 160 matrix) for 22 patients. T2-weighted images were acquired with either a conventional spin-echo sequence (repetition time [TR] millisecond / echo time [TE] millisecond, 2,000/80; two signals acquired, 256 × 160 matrix) for 16 patients or a fast spin-echo sequence (3,529–7,500 [mean, 5,212] / 65–80 [effective TR / effective TE], echo train length of 8, three signals acquired, 512 × 160 matrix) for 17 patients. For 11 of these 17 patients, respiratory triggering was used for the fast spin-echo sequence.

After SPIO enhancement, proton density-weighted and T2-weighted images with dual-echo sequences were obtained for all 41 patients: a conventional spin-echo sequence (repetition time [TR] millisecond / echo time [TE] millisecond, 1,800–2,000/15–20, 70–90; two signals acquired, 256 × 160 matrix) was done for 25 patients, and a respiratory-triggered fast spin-echo sequence (3,750–8,000 [mean, 4,974] / 20–40, 65–80 [effective TR / effective TE], echo train length of 8, three signals acquired, 512 × 160 matrix) for 16 patients. In 36 patients, T2*-weighted gradient echo images (fast spoiled gradient recalled acquisition in steady state or fast low angle shot; 140–150 / 10–12 / 60–70) were also obtained.

In 31 patients, ferumoxides (Feridex; Eiken Chemical, Tokyo, Japan) was administered at a dose of 10 μmol iron/kg body weight, diluted in 100 mL of a 5% glucose solution, and infused over 30 minutes. Imaging started 15–60 minutes from the end of the infusion. In 10 patients, SH U 555A (Resovist; Nihon Schering, Osaka, Japan), 4–16 μmol [mean, 10 μmol] iron/kg body weight, was injected as a rapid bolus, followed by saline solution flushing. Imaging started 10–40 minutes from the end of the injection.

CT Examination

Dynamic helical CT was performed with either the single (n = 29) or the double arterial phase imaging technique (n = 12). Both protocols included precontrast imaging and two- to four-phase imaging after bolus injection of a nonionic contrast agent at 300 mg iodine per mL (iopromide [Iopamiron 300; Nihon Schering] or iohexol [Omnipaque 300; Daiichi Pharmaceutical Co., Tokyo, Japan]) by a power injector (Autoenhance A-50; Nemoto Kyorindo, Tokyo, Japan) at a rate of 3–5 mL/s through a plastic catheter placed in the antecubital vein. The contrast agent was administered at a volume of 90–138 mL.

For the single arterial phase imaging technique (n = 29), a 1 second single-slice helical scanner (X-Vigor; Toshiba, Tokyo, Japan) or a 0.8 second single-slice helical scanner (HighSpeed Advantage; GE Medical Systems) was used. The parameters were 7 mm section collimation, 1.0–1.5 pitch, 7 mm reconstruction interval, 120 kVp, and 200–210 mA tube current. Triphasic (precontrast, arterial phase, and portal venous phase) or tetraphasic (triphasic plus equilibrium phase) dynamic helical CT imaging was also performed. Duration for each breath-hold helical CT scan was 17–25 seconds. The respective scanning delays for arterial phase, portal venous phase, and equilibrium phase images were 25, 70–100, and 150 seconds after the start of the contrast material injection.

For the double arterial phase imaging technique (n = 12), a half-second single-slice helical CT scanner (Aquilion; Toshiba) or a 0.8 second multislice helical CT scanner (LightSpeed QX/i; GE Medical Systems) was used. The parameters were 5 mm section collimation / 1.5 pitch (Aquilion) or 2.5 × 4 mm detector configuration / 6.0 pitch (LightSpeed QX/i), 5 mm thickness, 5 mm reconstruction interval, 120 kVp, and 270–400 mA tube current. Tetraphasic (precontrast, early arterial phase, late arterial phase, and equilibrium phase) or pentaphasic (tetraphasic plus portal venous phase) dynamic helical CT imaging was also performed. Intervals between the early arterial and the late arterial phase scanning were 5 seconds. Scanning duration from the beginning of the early arterial phase scanning to the end of the late arterial phase scanning during one breath hold was 26–34 seconds. The scanning time delay of 16.0–24.5 seconds (mean, 22.2 seconds) for early arterial phase imaging was determined by using an automatic bolus tracking technique (n = 3) or a test bolus technique (n = 9). The delay for the late arterial phase imaging was 31.5–45.5 seconds (mean, 38.9 seconds). The scanning delays for portal venous phase and equilibrium phase imaging were about 70 and 170 seconds, respectively, after the start of the contrast material injection. With the automatic bolus tracking technique, serial low-dose (50 mA) monitor scans were initiated 10 seconds after the start of injection of contrast material. Contrast enhancement was measured automatically in a region of interest defined in the abdominal aorta at the level of the starting position of the diagnostic scan. The trigger was set at an increase of 50 Hounsfield units in contrast enhancement of the abdominal aorta. Ten seconds after triggering, the early arterial phase helical CT scan was automatically started. With the test bolus technique, the scanning time delay was determined by using a test bolus (15 mL at 5 mL/s) of contrast medium followed by a series of single level CT scans at a low dose (120 kVp, 10 mA). The monitoring scans were acquired every 2 seconds from 10 seconds to 40 seconds. A cursor was placed over the abdominal aorta, and the time needed to reach peak aortic enhancement was used to determine the scan delay for early arterial phase imaging.

Imaging Assessment

Images from the combined MR sequences (all images available including those obtained before and after SPIO enhancement) and the combined CT images (all images available: precontrast, early arterial, late arterial, portal venous, and equilibrium phases images) were interpreted independently and separately by four blinded readers. These four readers were different from the two radiologists who decided the presence or absence of hypervascular HCC lesions based on some radiologic and pathologic findings. The readers had worked mainly as gastrointestinal radiologists for 6–13 years and had interpreted MRI of the liver as part of their daily clinical and research practice. They knew that the patients were at risk for HCC but did not have any other information about the patients' histories. The MR and CT images were viewed at separate sessions. Each reader recorded the presence and location of one or more hypervascular HCC lesions, assigning each a confidence rating on a four-point scale (1 = probably not a lesion, 2 = equivocal, 3 = probable lesion, 4 = definite lesion). At the time of scoring, the readers were aware that sensitivity calculations were made based on only those lesions awarded a confidence rating of 3 or 4. Nodules that met the criteria for hemangiomas, cysts, post-therapeutic lesions, or hypovascular lesions were eliminated from the data by the study coordinator after blind reading of the review procedure. The procedure was performed at two separate sessions, and at each, the images for all patients obtained with only one of the techniques were reviewed. The order of technique reviewed in each patient was randomized. The two reviewing sessions took place at an interval of 2 weeks.

Statistical Analysis

Alternative-free response receiver operating characteristic (AFROC) curve analysis was performed on a tumor-by-tumor basis. While the conventional ROC method

TABLE 1. *Area under the alternative-free response receiver operating characteristic curves (Az)*

Modality	Az value Reader 1	Reader 2	Reader 3	Reader 4	Mean
All lesions					
SPIO-enhanced MR	0.83	0.78	0.81	0.82	0.81*
Dynamic helical CT	0.79	0.73	0.80	0.74	0.76
Lesions less than or equal to 1 cm in diameter					
SPIO-enhanced MR	0.65	0.56	0.59	0.73	0.63
Dynamic helical CT	0.60	0.43	0.47	0.37	0.47
Lesions more than 1 cm in diameter					
SPIO-enhanced MR	0.95	0.94	0.97	Degeneracy**	0.95***
Dynamic helical CT	0.91	0.90	0.96	0.91	0.92

* The mean difference between MR imaging and CT was significant ($P < .05$).

** The data set was degenerate. In general, degeneracy should be found only in very small datasets or in those with many tied values.

*** The mean value was calculated from three Az values.

allows for only one response per image, the AFROC method allows for multiple responses per image (9). An AFROC curve was fitted to each reader's confidence rating by using a maximum-likelihood estimation program (ROCKIT 0.9B; courtesy of Metz CE, University of Chicago, 1998). The diagnostic performance of both techniques and readers was estimated by calculating the area under the AFROC curve (Az).

The sensitivity for each reader and each modality was determined by using only those lesions allocated a confidence rating of 3 or 4. The sensitivity derived from the mean of the results obtained from all four readers was also calculated.

For Az values, sensitivities, and positive predictive values (PPV), the statistical significance of any differences between CT and MRI was assessed by using the Student *t* test for paired data. A two-tailed P value of <0.05 was considered significant.

To assess interreader variability in image interpretation, the unweighted kappa statistic with binary data was used to measure the extent of agreement among the four readers. The binary data were calculated from the confidence rating value assigned to a true lesion by each of the readers. Binary values of 0 and 1 were assigned to lesions with a confidence rating value of ≤2 and ≥3, respectively. The extent of disagreement was not factored into the calculation. Kappa values larger than 0 were considered to indicate a positive correlation; values up to 0.40 indicated positive but poor agreement; values of 0.41–0.75, good agreement; and values greater than 0.75, excellent agreement.

RESULTS

Alternative-free Response ROC Analysis

The Az values determined by the reader for SPIO-enhanced MRI and dynamic helical CT are shown in Table 1. For each of the readers, almost all Az values for SPIO-enhanced MRI were greater than those for dynamic helical CT for all lesions (n = 52), for those less than or equal to 1 cm in diameter (n = 14), and for those more than 1 cm in diameter (n = 38). The diagnostic accuracy in the detection of hypervascular HCC with SPIO-enhanced MRI (mean Az = 0.81) was significantly higher than that with dynamic helical CT (mean Az = 0.76, $p < 0.05$).

Sensitivity

The sensitivities for the detection of hypervascular HCC by technique are shown in Table 2. Each reader

TABLE 2. *Sensitivity for revealing hypervascular hepatocellular carcinoma*

Modality	Reader 1	Reader 2	Reader 3	Reader 4	Mean*
All lesions (N = 52)					
SPIO-enhanced MR	0.77 (40)	0.77 (40)	0.69 (36)	0.75 (39)	0.75
Dynamic helical CT	0.75 (39)	0.69 (36)	0.69 (36)	0.71 (37)	0.71
Lesions less than or equal to 1 cm diameter (N = 14)					
SPIO-enhanced MR	0.43 (6)	0.50 (7)	0.21 (3)	0.50 (7)	0.41
Dynamic helical CT	0.43 (6)	0.36 (5)	0.29 (4)	0.29 (4)	0.34
Lesions more than 1 cm diameter (N = 38)					
SPIO-enhanced MR	0.89 (34)	0.87 (33)	0.87 (33)	0.84 (32)	0.87
Dynamic helical CT	0.87 (33)	0.82 (31)	0.84 (32)	0.87 (33)	0.85

Numbers of detected tumors are shown in parentheses.

* The mean differences between MR imaging and CT were not significant ($P = 0.13$, 0.35, and 0.32).

TABLE 3. *Positive predictive values for revealing hypervascular hepatocellular carcinoma*

Modality	Reader 1	Reader 2	Reader 3	Reader 4	Mean*
All lesions					
SPIO-enhanced MR	0.71 (16)	0.71 (16)	0.94 (2)	0.93 (3)	0.83
Dynamic helical CT	0.74 (14)	0.65 (19)	0.92 (3)	0.86 (6)	0.79
Lesions less than or equal to 1 cm diameter					
SPIO-enhanced MR	0.32 (13)	0.35 (13)	0.75 (1)	0.70 (3)	0.53
Dynamic helical CT	0.43 (8)	0.28 (13)	0.67 (2)	0.67 (2)	0.51
Lesions more than 1 cm diameter					
SPIO-enhanced MR	0.92 (3)	0.92 (3)	0.97 (1)	1.00 (0)	0.95
Dynamic helical CT	0.85 (6)	0.84 (6)	0.97 (1)	0.89 (4)	0.89

Numbers of false positive lesions are shown in parentheses.
* The mean differences between MR imaging and CT were not significant ($P = 0.21$, 0.70, and 0.06).

rated the sensitivity of SPIO-enhanced MRI higher than or equal to that of dynamic helical CT for all lesions. However, there was no statistical significant difference between the mean sensitivity of SPIO-enhanced MRI and of dynamic helical CT.

False-positive Lesions

The number of false-positive lesions and the PPV by reader and by technique are shown in Table 3. For all four readers using either technique, the majority of false-positive lesions were less than or equal to 1 cm in diameter. Most PPVs for SPIO-enhanced MRI were greater than those of dynamic helical CT (Fig. 1), although there was no statistical significant difference between the mean PPV of SPIO-enhanced MRI and of dynamic helical CT.

False-negative Lesions

None of the readers detected five nodules in four patients with either SPIO-enhanced MRI or dynamic helical CT. With SPIO-enhanced MRI, seven nodules in six patients were not detected by any of the readers, although two of these nodules in two patients were detected with dynamic helical CT by at least one reader (Fig. 2). With dynamic helical CT, 10 nodules in 8 patients were not detected by any of the readers, while 5 of these nodules in 5 patients were detected with SPIO-enhanced MRI by at least one reader (Fig. 3).

Interreader Variability

The kappa values for the four readers calculated based on each reader's confidence levels for the AFROC analysis were 0.87 for SPIO-enhanced MRI and 0.92 for dynamic helical CT. Excellent agreement was obtained

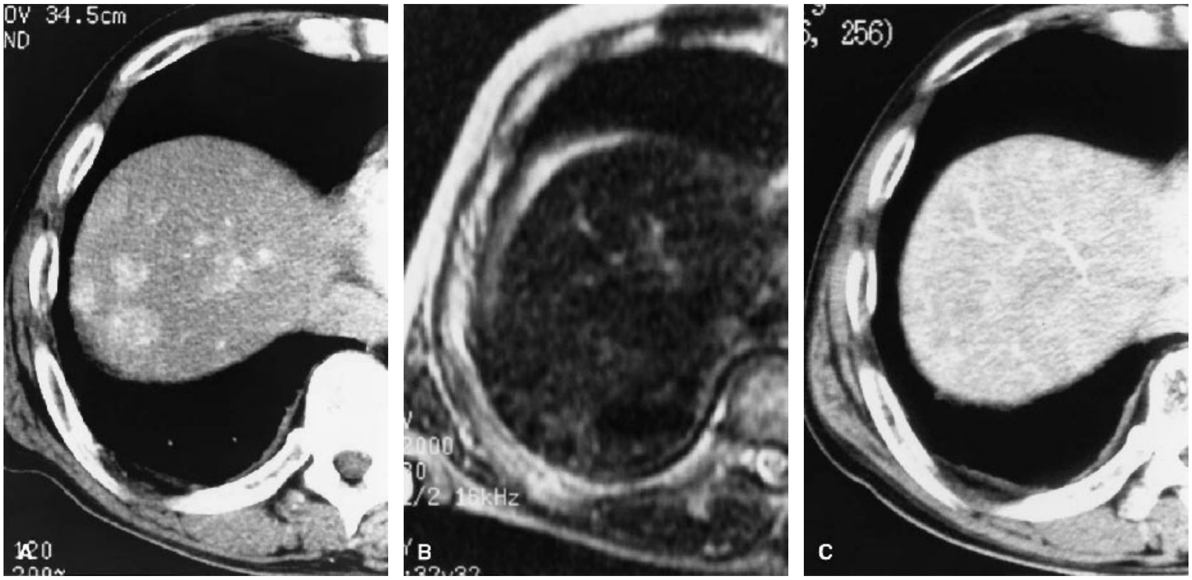

FIG. 1. Images obtained from a 71-year-old man. **A:** On dynamic helical CT arterial phase images, multiple hyperattenuated areas are seen in the dome of the liver. **B:** SPIO-enhanced spin-echo T2-weighted image (TR/TE = 2,000/80) does not show the lesions. **C:** No lesions are seen in CT arterial portography image, either. In addition, no tumor stains were observed with digital subtraction hepatic arteriography, so that the multiple hyperattenuated areas seen on dynamic helical CT were judged to be pseudolesions due to perfusion abnormality.

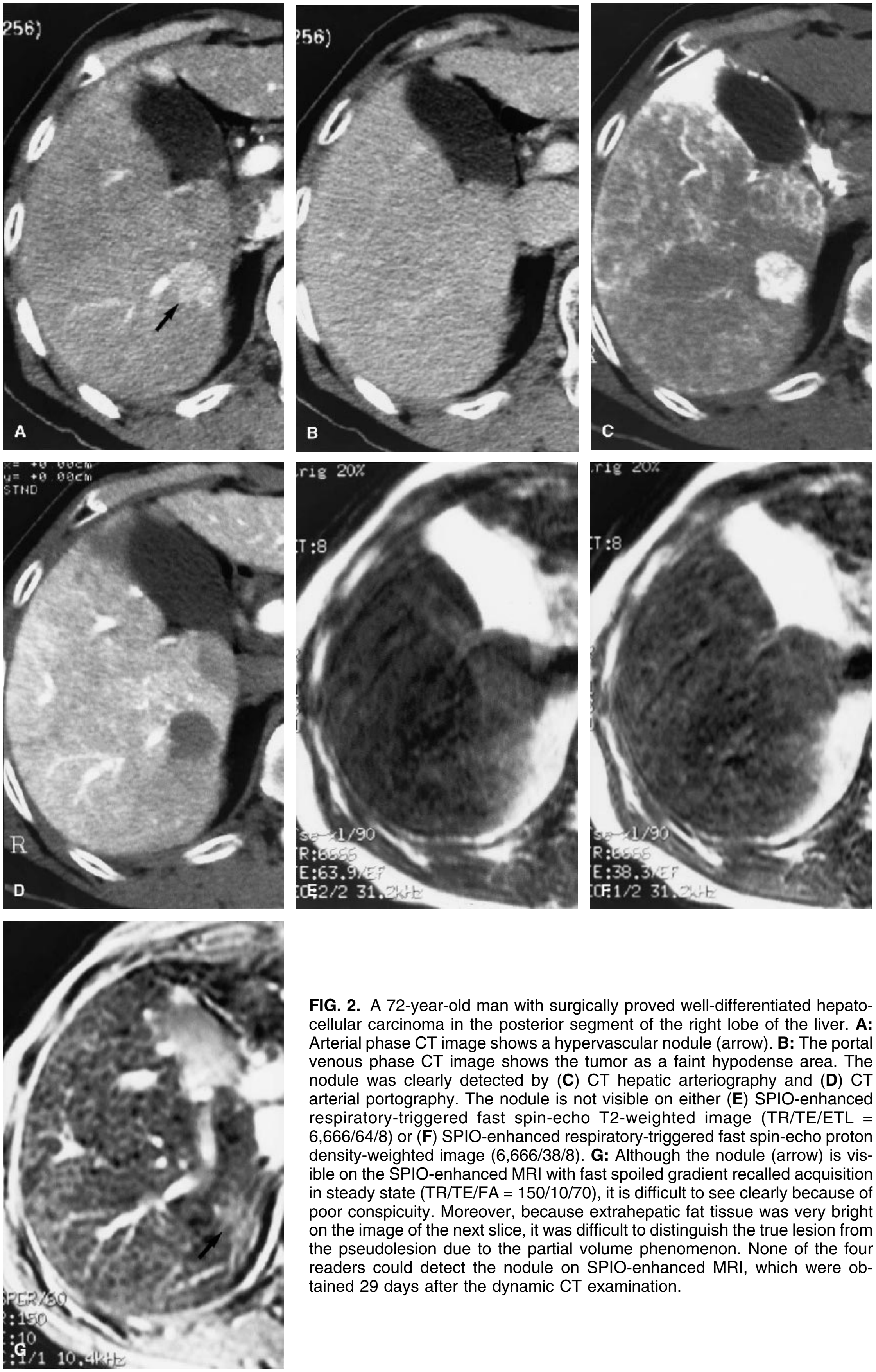

FIG. 2. A 72-year-old man with surgically proved well-differentiated hepatocellular carcinoma in the posterior segment of the right lobe of the liver. **A:** Arterial phase CT image shows a hypervascular nodule (arrow). **B:** The portal venous phase CT image shows the tumor as a faint hypodense area. The nodule was clearly detected by (**C**) CT hepatic arteriography and (**D**) CT arterial portography. The nodule is not visible on either (**E**) SPIO-enhanced respiratory-triggered fast spin-echo T2-weighted image (TR/TE/ETL = 6,666/64/8) or (**F**) SPIO-enhanced respiratory-triggered fast spin-echo proton density-weighted image (6,666/38/8). **G:** Although the nodule (arrow) is visible on the SPIO-enhanced MRI with fast spoiled gradient recalled acquisition in steady state (TR/TE/FA = 150/10/70), it is difficult to see clearly because of poor conspicuity. Moreover, because extrahepatic fat tissue was very bright on the image of the next slice, it was difficult to distinguish the true lesion from the pseudolesion due to the partial volume phenomenon. None of the four readers could detect the nodule on SPIO-enhanced MRI, which were obtained 29 days after the dynamic CT examination.

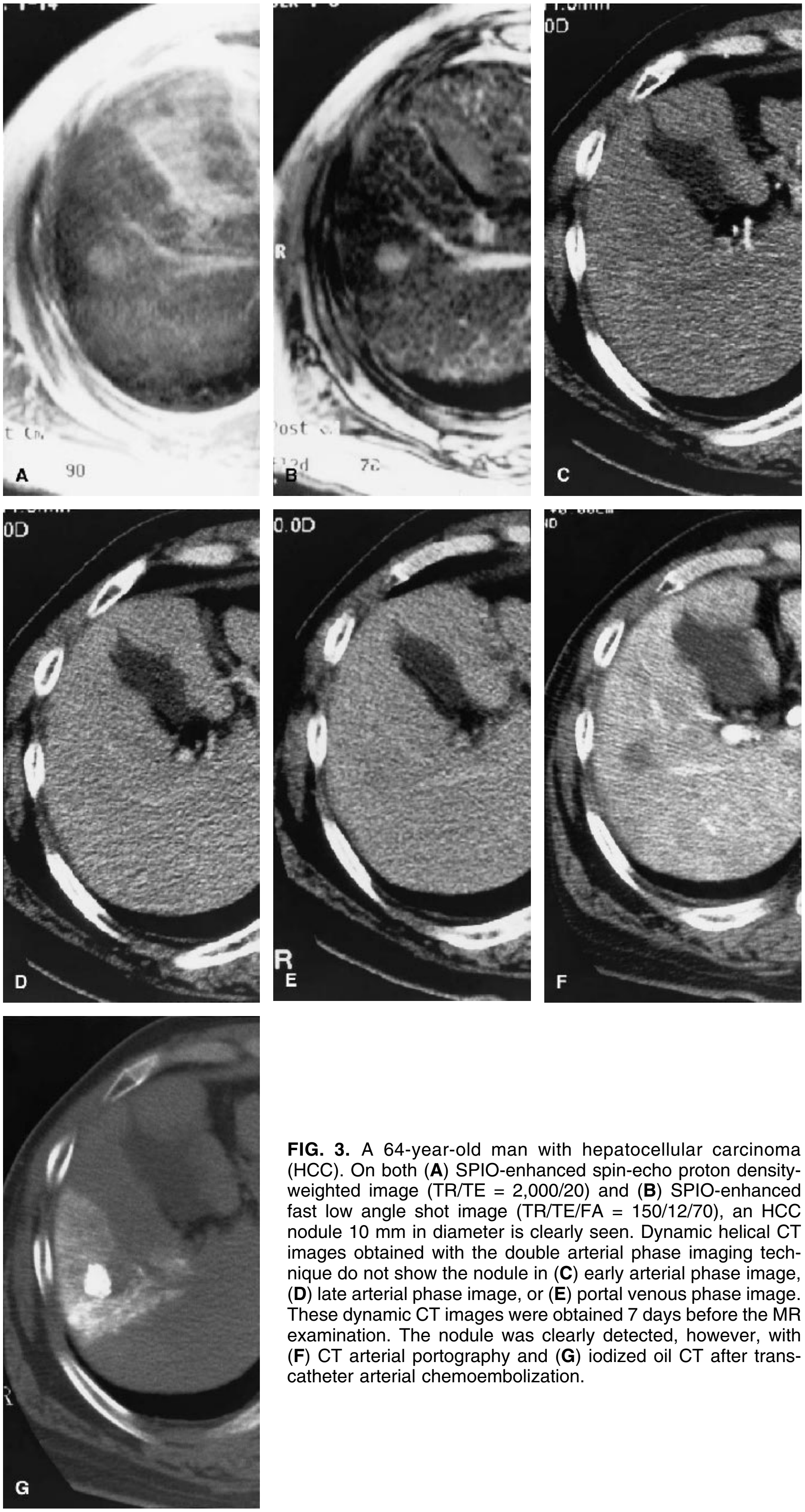

FIG. 3. A 64-year-old man with hepatocellular carcinoma (HCC). On both (**A**) SPIO-enhanced spin-echo proton density-weighted image (TR/TE = 2,000/20) and (**B**) SPIO-enhanced fast low angle shot image (TR/TE/FA = 150/12/70), an HCC nodule 10 mm in diameter is clearly seen. Dynamic helical CT images obtained with the double arterial phase imaging technique do not show the nodule in (**C**) early arterial phase image, (**D**) late arterial phase image, or (**E**) portal venous phase image. These dynamic CT images were obtained 7 days before the MR examination. The nodule was clearly detected, however, with (**F**) CT arterial portography and (**G**) iodized oil CT after transcatheter arterial chemoembolization.

among the four readers with regard to the presence of lesions.

DISCUSSION

In this study, we evaluated the diagnostic capabilities of dynamic helical CT and SPIO-enhanced MRI to detect only hypervascular HCCs, which are fed mainly by the hepatic artery. Targeted transarterial oily chemoembolization can be used for hypervascular HCCs and is reported to have a low local recurrence rate and cause minimum damage to the nontumorous liver parenchyma (10). The detection of hypervascular HCCs is significant for planning treatment when transarterial chemoembolization therapy is being considered because it is usually effective only for hypervascular HCC (11,12). Dynamic CT and dynamic gadolinium-enhanced MRI are useful for the detection of such lesions (6) because they are usually enhanced compared with the surrounding liver parenchyma during arterial phase scanning. The diagnostic capability of SPIO-enhanced MRI is thought to be better for the detection of hypervascular HCCs, which tend to be moderately or poorly differentiated (13), than of hypovascular ones. The reason for this is that the conspicuity of nodules on SPIO-enhanced MRI depends on differences in the number of Kupffer cells within a nodule and the surrounding liver (14), and the differences are generally greater for poorly or moderately differentiated HCCs than for well-differentiated ones (15).

Our results showed higher Az values, comparable detection sensitivity, and a comparable number of false-positive findings for the detection of hypervascular HCC by SPIO-enhanced MRI than by dynamic helical CT. This finding can be explained by the fact that hypervascular tumor nodules cannot always be easily detected on dynamic helical CT because of inappropriate scanning timing for arterial phase imaging or modest hypervascularity of the tumor, while some of those nodules can be clearly seen on SPIO-enhanced MRI as we showed in Figure 3, and nontumorous perfusion abnormalities, such as arterioportal shunt, may mimic hypervascular tumors on dynamic helical CT, especially in patients with cirrhotic liver (16), as we showed in Figure 1. It can also cause false-negative findings with dynamic helical CT that nontumorous perfusion abnormalities are common because radiologists sometimes incorrectly diagnose true hypervascular HCC as pseudolesions. Although some nontumorous arterioportal shunts may show high intensity on SPIO-enhanced MRI, it is a rare finding compared with hypervascular tumors or tumorous arterioportal shunts (17).

Choi et al. (18) reported that SPIO-enhanced MRI had the same diagnostic accuracy for the detection of HCC as combined helical CT arterial portography and CT hepatic arteriography. It was also reported that combined helical CT arterial portography and CT hepatic arteriography showed superior HCC detection to that by dynamic helical CT (19) or dynamic gadolinium-enhanced MRI (19,20). Thus, our data are in agreement with these results. However, Tang et al. (5) reported that SPIO-enhanced MRI was less diagnostically accurate than dynamic gadolinium-enhanced MRI. This seems to be incompatible with our and others' findings because some researchers (6) showed similar diagnostic capability for the detection of HCC by dynamic helical CT and dynamic gadolinium-enhanced MRI. It seems that the study by Tang et al. was restricted in its ability to evaluate diagnostic accuracy because of the method they used. They used 68 images with lesions and selected another 68 images without lesions to match the distribution of anatomic levels depicted in the 68 images with lesions. This total of 136 images was only part of all the images obtained from their 53 patients. In patients with cirrhotic liver, nontumorous arterioportal shunts mimicking hypervascular tumors can often be seen in dynamic studies (16) and can cause false-positive findings, especially with dynamic CT or dynamic gadolinium-enhanced MRI. However, the study by Tang et al. showed no evidence that images with arterioportal shunts were fairly selected. Avoiding the selection of images with arterioportal shunts would be highly advantageous for the evaluation of dynamic studies. On the other hand, we used the AFROC method, which allows multiple responses per image so that we could evaluate all the images from our 41 patients. Therefore, we think our method was fair in terms of the SPIO-enhanced MRI and the dynamic study.

Another possible reason for the incompatibility of our data and those by Tang et al. is the difference in patient population. As for severity of cirrhosis, only 2 of our 41 patients were classified as Child-Pugh class C in our study, whereas 13 of the 53 patients in the study by Tang et al. were class C. Cirrhotic liver tissue shows less response to SPIO particles than does healthy liver tissue (4), so the diagnostic capability of SPIO-enhanced MRI for HCC detection would be limited in patients with severe cirrhosis. Even with CT, however, detection of HCC in patients with cirrhotic liver would also be difficult because of fibrosis, regenerative nodules, decreased portal blood flow from portal hypertension (21), and arterioportal shunt. Lim et al. (22) studied transplantation patients and concluded that dynamic helical CT was relatively insensitive for HCC detection in those with cirrhotic livers. Therefore, it appears that severe cirrhosis cannot necessarily explain the inferior diagnostic capability of SPIO-enhanced MRI compared with that of dynamic helical CT or dynamic gadolinium-enhanced MRI.

Recently, Pauleit et al. (23) also reported that dynamic gadolinium-enhanced MRI was more diagnostically accurate than SPIO-enhanced MRI in the detection of small HCC by using AFROC method. However, we think that the pulse sequence they used was not necessarily optimized for SPIO-enhanced MRI. After SPIO enhancement, they obtained images only with respiratory-triggered T2-weighted turbo spin-echo sequence. Ward et al. (24) compared various SPIO-enhanced images and found that T2-weighted fast spin-echo sequence was the least accurate among them in the detection of liver tumors, though their scanner was operated at 1.0 T. They concluded that spin-echo sequence with dual-echo technique and gradient echo sequence were the most accurate sequences after SPIO enhancement. In our study, we obtained proton density-weighted and T2-weighted images with dual-echo sequences for all 41 patients, and we also obtained T2*-weighted gradient echo images in 36 of 41 patients. We think that our protocol for SPIO-enhanced MRI is probably better than that of Pauleit et al.

Hypovascular nodules tend to be well-differentiated HCC or dysplastic nodules (13) with variable arterial and portal blood supplies (13,25) and no significant differences in the number of Kupffer cell (15). Thus, detection and characterization of hypovascular lesions is sometimes difficult even with dynamic CT, dynamic gadolinium-enhanced MRI, or SPIO-enhanced MRI. In such cases, percutaneous biopsy with sonographic or CT guidance may be needed for a definitive diagnosis, although this technique entails some problems, too, such as lesion heterogeneity, difficulty in obtaining a sufficient tissue sample, or its invasiveness (13). Since differential diagnosis among hypovascular lesions is obviously of clinical importance, we think that further study of hypovascular lesions is needed.

Some limitations of our study require consideration. First, histopathologic proof was obtained from only 25 of the 36 patients with HCC. Thus, it is possible that some false-positive lesions may have been included inadvertently. However, we carefully evaluated many imaging findings, including dynamic gadolinium-enhanced MRI, angiographically assisted CT, iodized oil CT, and follow-up CT and MRI to identify true lesions. Therefore, we think we were able to exclude most false-positive lesions. Second, no histopathologic proof of the absence of lesions in the nonresected portion of the liver was obtained. This is not a significant limitation, however, since we evaluated only hypervascular lesions, which would appear on digital subtraction angiography or angiographically assisted CT. Third, double arterial phase helical CT imaging was used for only 12 of our 41 patients. Because double arterial phase imaging with multislice helical CT (26,27) reportedly improves diagnostic performance for the detection of hypervascular tumors, further study of the difference in the diagnostic capabilities of SPIO-enhanced MRI and dynamic multislice helical CT is needed, although SPIO-enhanced MRI sometimes showed hypervascular HCC more clearly than did double arterial phase CT imaging, as we showed in Figure 3. Fourth, some MRI protocols and some dynamic helical CT imaging protocols were used in our study for the detection of HCC because we used some different imaging units. However, our protocols did not deviate from currently accepted protocols for the detection of HCC.

In conclusion, SPIO-enhanced MRI showed a slightly higher diagnostic accuracy than dynamic helical CT for the detection of hypervascular HCC. SPIO-enhanced MRI should therefore be considered as a useful diagnostic technique for the detection of hypervascular HCC occurring in patients with chronic liver disease.

REFERENCES

1. Muller RD, Vogel K, Neumann K, et al. SPIO-MR imaging versus double-phase spiral CT in detecting malignant lesions of the liver. *Acta Radiol* 1999;40:628–35.
2. Bluemke DA, Paulson EK, Choti MA, et al. Detection of hepatic lesions in candidates for surgery: comparison of ferumoxides-enhanced MR imaging and dual-phase helical CT. *AJR Am J Roentgenol* 2000;175:1653–8.
3. Reimer P, Jahnke N, Fiebich M, et al. Hepatic lesion detection and characterization: value of nonenhanced MR imaging, superparamagnetic iron oxide-enhanced MR imaging, and spiral CT-ROC analysis. *Radiology* 2000;217:152–8.
4. Elizondo G, Weissleder R, Stark DD, et al. Hepatic cirrhosis and hepatitis: MR imaging enhanced with superparamagnetic iron oxide. *Radiology* 1990;174:797–801.
5. Tang Y, Yamashita Y, Arakawa A, et al. Detection of hepatocellular carcinoma arising in cirrhotic livers: comparison of gadolinium- and ferumoxides-enhanced MR imaging. *AJR Am J Roentgenol* 1999;172:1547–54.
6. Kim T, Murakami T, Oi H, et al. Detection of hypervascular hepatocellular carcinoma by dynamic MRI and dynamic spiral CT. *J Comput Assist Tomogr* 1995;19:948–54.
7. Yamashita Y, Mitsuzaki K, Yi T, et al. Small hepatocellular carcinoma in patients with chronic liver damage: prospective comparison of detection with dynamic MR imaging and helical CT of the whole liver. *Radiology* 1996;200:79–84.
8. Pugh RN, Murray-Lyon IM, Dawson JL, et al. Transection of the esophagus for bleeding esophageal varices. *Br J Surg* 1973;60: 646–9.
9. Chakraborty DP, Winter LH. Free-response methodology: alternate analysis and a new observer-performance experiment. *Radiology* 1990;174:873–81.
10. Takayasu K, Muramatsu Y, Maeda T, et al. Targeted transarterial oily chemoembolization for small foci of hepatocellular carcinoma using a unified helical CT and angiography system: analysis of factors affecting local recurrence and survival rates. *AJR Am J Roentgenol* 2001;176:681–8.
11. Ohishi H, Uchida H, Yoshimura H, et al. Hepatocellular carcinoma detected by iodized oil. Use of anticancer agents. *Radiology* 1985; 154:25–9.
12. Yumoto Y, Jinno K, Tokuyama K, et al. Hepatocellular carcinoma detected by iodized oil. *Radiology* 1985;154:19–24.
13. Hayashi M, Matsui O, Ueda K, et al. Correlation between the blood supply and grade of malignancy of hepatocellular nodules associated with liver cirrhosis: evaluation by CT during intraarterial injection of contrast medium. *AJR Am J Roentgenol* 1999;172: 969–76.
14. Lim JH, Choi D, Cho SK, et al. Conspicuity of hepatocellular nodular lesions in cirrhotic livers at ferumoxides-enhanced MR imaging: importance of Kupffer cell number. *Radiology* 2001;220: 669–76.
15. Imai Y, Murakami T, Yoshida S, et al. Superparamagnetic iron oxide-enhanced magnetic resonance images of hepatocellular carcinoma: correlation with histologic grading. *Hepatology* 2000;32: 205–12.
16. Kim TK, Choi BI, Han JK, et al. Nontumorous arterioportal shunt mimicking hypervascular tumor in cirrhotic liver: two-phase spiral CT findings. *Radiology* 1998;208:597–603.
17. Mori K, Yoshioka H, Itai Y, et al. Arterioportal shunts in cirrhotic patients: evaluation of the difference between tumorous and nontumorous arterioportal shunts on MR imaging with superparamagnetic iron oxide. *AJR Am J Roentgenol* 2000;175:1659–64.
18. Choi D, Kim S, Lim J, et al. Preoperative detection of hepatocellular carcinoma: ferumoxides-enhanced MR imaging versus combined helical CT during arterial portography and CT hepatic arteriography. *AJR Am J Roentgenol* 2001;176:475–82.

19. Hori M, Murakami T, Oi H, et al. Sensitivity in detection of hypervascular hepatocellular carcinoma by helical CT with intra-arterial injection of contrast medium, and by helical CT and MR imaging with intravenous injection of contrast medium. *Acta Radiol* 1998;39:144–51.
20. Kanematsu M, Hoshi H, Murakami T, et al. Detection of hepatocellular carcinoma in patients with cirrhosis: MR imaging versus angiographically assisted helical CT. *AJR Am J Roentgenol* 1997;169:1507–15.
21. Miller WJ, Baron RL, Dodd GD III, et al. Malignancies in patients with cirrhosis: CT sensitivity and specificity in 200 consecutive transplant patients. *Radiology* 1994;193:645–50.
22. Lim JH, Kim CK, Lee WJ, et al. Detection of hepatocellular carcinomas and dysplastic nodules in cirrhotic livers: accuracy of helical CT in transplant patients. *AJR Am J Roentgenol* 2000;175:693–8.
23. Pauleit D, Textor J, Bachmann R, et al. Hepatocellular carcinoma: detection with gadolinium- and ferumoxides-enhanced MR imaging of the liver. *Radiology* 2002;222:73–80.
24. Ward J, Chen F, Guthrie JA, et al. Hepatic lesion detection after superparamagnetic iron oxide enhancement: comparison of five T2-weighted sequences at 1.0 T by using alternative-free response receiver operating characteristic analysis. *Radiology* 2000;214:159–66.
25. Lim JH, Cho JM, Kim EY, et al. Dysplastic nodules in liver cirrhosis: evaluation of hemodynamics with CT during arterial portography and CT hepatic arteriography. *Radiology* 2000;214:869–74.
26. Foley WD, Mallisee TA, Hohenwalter MD, et al. Multiphase hepatic CT with a multirow detector CT scanner. *AJR Am J Roentgenol* 2000;175:679–85.
27. Murakami T, Kim T, Takamura M, et al. Hypervascular hepatocellular carcinoma: detection with double arterial phase multidetector row helical CT. *Radiology* 2001;218:763–7.